

Mechanistic insight into competing precipitation behaviors of phosphorus and oxygen in heavily phosphorus-doped Czochralski silicon

Cite as: J. Appl. Phys. 138, 125703 (2025); doi: 10.1063/5.0292095

Submitted: 21 July 2025 · Accepted: 5 September 2025 ·

Published Online: 22 September 2025



View Online



Export Citation



CrossMark

Defan Wu,^{1,2} Tong Zhao,^{1,3} Xingbo Liang,⁴ Tianqi Deng,² Hao Chen,¹ Qunlin Nie,¹ Bin Ye,⁴ Shenzhong Li,^{1,4} Daxi Tian,⁴ Deren Yang,^{1,3} and Xiangyang Ma^{1,3,a}

AFFILIATIONS

¹State Key Laboratory of Silicon and Advanced Semiconductor Materials and School of Materials Science and Engineering, Zhejiang University, Hangzhou 310027, China

²Zhejiang Provincial Key Laboratory of Power Semiconductor Materials and Devices, ZJU-Hangzhou Global Scientific and Technological Innovation Center, Hangzhou, Zhejiang 311200, China

³Shangyu Institute of Semiconductor Materials, Zhejiang University, Shaoxing 212399, China

⁴QL Electronics Science (Quzhou) Co., Ltd., No. 52, Panlong South Road, Quzhou 324000, China

^aAuthor to whom correspondence should be addressed: mxyoung@zju.edu.cn

ABSTRACT

Heavily phosphorus-doped Czochralski (HP-Cz) silicon is a critical substrate material for power electronic devices. Its supersaturated phosphorus and oxygen impurities can precipitate during the device thermal processing, degrading the carrier concentration stability. This work systematically investigates the thermodynamics and kinetics of phosphorus precipitation and oxygen precipitation in HP-Cz silicon ($\sim 1 \text{ m}\Omega \cdot \text{cm}$) annealed at 850–1050 °C. Thermodynamic analyses reveal that phosphorus precipitation dominates initially at each temperature due to its smaller critical nucleation radius and higher nucleation rate, experimentally verified by the decrease in carrier concentration due to silicon phosphide (SiP) precipitate formation. However, oxygen precipitation becomes increasingly significant with the prolonged annealing time, triggering the dissolution of pre-formed SiP precipitates via two distinct density functional theory-validated mechanisms: oxidative dissolution by the interstitial oxygen impurities and decomposition mediated by the silicon interstitials generated by oxygen precipitation. The SiP precipitate dissolution leads to the gradual recovery of carrier concentration, reaching nearly complete recovery after 128 h at 950 °C or 16 h at 1050 °C, but remaining incomplete after 128 h at 850 °C due to phosphorus trapping within the oxide precipitates. Transmission electron microscopy (TEM) provides direct evidence of oxygen precipitation heterogeneously nucleating on the pre-existing SiP precipitates at 850 and 950 °C. Furthermore, systematic TEM characterization reveals a temperature-dependent morphological evolution of oxide precipitates: from hexagonal platelets (850 °C) to quadrangular platelets (950 °C) and finally to octahedral/truncated octahedral geometries (1050 °C), consistent with the energy-minimization principles. Collectively, this work elucidates the competing thermodynamics and kinetics governing phosphorus and oxygen precipitation, providing a fundamental understanding of impurity interactions and carrier concentration evolution critical for optimizing the processes of devices using HP-Cz silicon.

© 2025 Author(s). All article content, except where otherwise noted, is licensed under a Creative Commons Attribution (CC BY) license (<https://creativecommons.org/licenses/by/4.0/>). <https://doi.org/10.1063/5.0292095>

04 October 2025 06:19:18

I. INTRODUCTION

Heavily phosphorus-doped Czochralski (HP-Cz) silicon wafers are predominantly used as the substrates of epitaxial silicon wafers, which serve as the base materials for power electronic devices such as Schottky diodes and metal-oxide-semiconductor

field effect transistors (MOSFETs). To minimize the on-resistance of such power devices, the substrate resistivity needs to be reduced as much as possible.^{1–5} Presently, the commercially available HP-Cz silicon wafers can achieve the resistivities as low as $\sim 1 \text{ m}\Omega \cdot \text{cm}$. The phosphorus impurities in such heavily doped

wafers can become supersaturated at the thermal processing temperatures typical of device fabrication.^{6–8} Our previous work has demonstrated that the phosphorus impurities in the HP-Cz silicon wafers with a resistivity of $\sim 1 \text{ m}\Omega \cdot \text{cm}$ can precipitate out to form orthorhombic silicon phosphide (SiP) precipitates during the crystal growth of HP-Cz silicon and the post-growth anneal at temperatures ranging from 450 to 1050 °C.⁹ Such phosphorus precipitation, occurring across the aforementioned temperature range, coincides with a decrease in carrier concentration,^{9,10} because a number of substitutional phosphorus atoms, which act as the donors in silicon, are removed from the lattice.

Oxygen precipitation in Cz silicon wafers, when appropriately controlled, has been shown to enhance mechanical strength, reduce warpage, and offer internal gettering sites for metallic impurities, thereby improving the device reliability.^{11–14} Although extensively studied in lightly doped Cz silicon,^{15–19} oxygen precipitation in HP-Cz silicon has received limited investigation.^{20,21} Early study indicated that heavy phosphorus-doping exerted a negligible effect on oxygen precipitation.²² However, the subsequent investigations revealed the contradictory trends. Zeng *et al.* reported the heterogeneous nucleation of oxygen precipitation on the pre-existing SiP precipitates during a low-high two-step anneal, demonstrating the enhanced oxygen precipitation in HP-Cz silicon with a phosphorus concentration of $4.6 \times 10^{19} \text{ cm}^{-3}$.²³ In contrast, Porrini *et al.* observed the significant suppression of oxygen precipitation in HP-Cz silicon with the phosphorus concentrations above $2.9 \times 10^{19} \text{ cm}^{-3}$.²⁴ These conflicting findings underscore the unresolved complexity of oxygen precipitation behavior in HP-Cz silicon.

Since both phosphorus and oxygen impurities in HP-Cz silicon wafers are supersaturated at the typical device processing temperatures (e.g., 800–1100 °C), the precipitation of these impurities can occur during the thermal treatments at such temperatures.^{2,25,26} This naturally raises the following critical questions: (1) Is there a temporal sequence between phosphorus precipitation and oxygen precipitation? (2) What correlation exists between phosphorus precipitation and oxygen precipitation? (3) How do the coexisting SiP and silicon oxide (SiO_x) precipitates interact? How do the dual precipitation processes influence the carrier concentration in HP-Cz silicon?

To address the above questions, we combine the experimental investigations and theoretical calculations to study the precipitation behaviors of phosphorus and oxygen in HP-Cz silicon during the prolonged anneal at 850–1050 °C. We find that phosphorus precipitation predominates over oxygen precipitation during the early stage isothermal anneal at each temperature, resulting in the decrease in carrier concentration. With the extension of isothermal anneal, however, oxygen precipitation becomes increasingly significant while the preformed SiP precipitates are progressively dissolved, leading to the gradual recovery of carrier concentration. Based on density functional theory (DFT) calculations, we propose two dissolution mechanisms of SiP precipitates: oxidative dissolution by oxygen impurities and decomposition mediated by the silicon interstitials generated by oxygen precipitation. Moreover, the heterogeneous nucleation onto the preformed SiP precipitate for the subsequent oxygen precipitation at 850 or 950 °C is directly visualized by transmission electron microscopy (TEM). It is

believed that this work gives an insight into the competing precipitation behaviors of phosphorus and oxygen in HP-Cz silicon.

II. EXPERIMENTAL

One 300 mm-diameter, $\langle 100 \rangle$ -oriented, double-sided mirror-polished HP-Cz silicon wafer with a resistivity of $\sim 1 \text{ m}\Omega \cdot \text{cm}$ was employed. The phosphorus and oxygen concentrations, as measured by secondary ion mass spectrometry (SIMS) using a Cameca IMS 7f-Auto system, were 7.35×10^{19} and $7.79 \times 10^{17} \text{ cm}^{-3}$, respectively. Multiple $15 \times 15 \text{ mm}^2$ sized specimens were cleaved from this HP-Cz silicon wafer for different annealing schemes. All specimens received an initial homogenization anneal at 1250 °C for 30 min in an argon atmosphere to eliminate the thermal history effects. For brevity, this homogenization step will not be explicitly referenced in the subsequent descriptions. Following the homogenization anneal, the specimens were isothermally annealed at 850–1050 °C for different durations up to 128 h. For each isothermal anneal, three specimens were cleaved from the adjacent areas within the HP-Cz silicon wafer.

The carrier (electron) concentrations in the HP-Cz silicon specimens were measured by a Lakeshore 7604 Hall effect measurement system with Van Der Pauw configuration. Before and after each isothermal anneal, the carrier concentrations in the three specimens as mentioned above were measured. To ensure the statistical reliability, five Hall effect measurements were performed on each specimen before and after each isothermal anneal, respectively. After Hall effect measurement, one of the three annealed specimen was preferentially etched in Yang1 etchant [HF (49%): CrO_3 (0.5 M) = 1:1 in volume ratio] at room temperature for 10 min, followed by the observation using an Olympus MX50 optical microscope (OM) equipped with a CCD camera. The average precipitate density was determined from the measurements conducted at six randomly selected areas on the preferentially etched cleavage plane of the annealed specimen. For the microscopic characterization of the precipitates formed by different isothermal anneals, the annealed specimens were first thinned to be electronically transparent by successive mechanical thinning and ion-milling. Subsequently, they were characterized with a FEI Tecnai G2 F20 S-Twin electron microscope operated at 200 kV, equipped with an energy dispersive spectrometry (EDS) system.

III. THEORETICAL CALCULATIONS

The structure and energy of the supercell for the interface between the SiP precipitate and the silicon matrix, denoted as SiP/Si interface, were calculated using the plane-wave pseudopotential method within the density functional theory (DFT), as implemented in the Vienna *Ab initio* Simulation Package (VASP).²⁷ Herein, the SiP/Si interface was composed based on the HRTEM result reported in our previous work,⁹ in which the $\{010\}$ planes of the orthorhombic SiP precipitate is found to be parallel to the $\{111\}$ planes of the silicon matrix.⁹ In this work, the incorporation of additional oxygen or silicon atom to the SiP/Si interface was addressed by the DFT calculations. The generalized gradient approximation (GGA) was used for the exchange and correlation function. A $3 \times 2 \times 1 \text{ k}$ point sampling of the Brillouin zone and a plane-wave basis set with a cutoff energy of 450 eV were

employed.²⁸ All atoms are fully relaxed using the conjugate gradient method to minimize the total energy until all residual forces on each constituent atom become smaller than 0.03 eV/Å. All structures were visualized using VESTA.²⁹

IV. RESULTS AND DISCUSSION

A. Thermodynamic analyses on oxygen precipitation and phosphorus precipitation

Given the supersaturation of both oxygen and phosphorus impurities in HP-Cz silicon at temperatures up to 1050 °C, both impurities can precipitate during the isothermal anneal. To determine which precipitation process dominates thermodynamically, comparative thermodynamic analysis of critical nucleation radii and temperature-dependent nucleation rates is required. According to the classical thermodynamical theory, the change in the free energy (ΔG) due to the precipitation of certain impurities out of the HP-Cz silicon matrix can be expressed as^{30–32}

$$\Delta G = -\frac{4}{3}\pi r^3(\Delta G_v - \Delta G_s) + 4\pi r^2\gamma, \quad (1)$$

where ΔG_v is the decrease in free energy per unit volume, ΔG_s is the increase in strain energy per unit volume, and γ is the interface energy per unit area. Then, the critical radius (r_c), nucleation barrier (ΔG_c), and the steady-state nucleation rate (J) for the formation of precipitates in HP-CZ silicon can be deduced as

$$r_c = \frac{2\gamma}{\Delta G_v - \Delta G_s}, \quad (2)$$

$$\Delta G_c = \frac{4\pi\gamma r_c^2}{3}, \quad (3)$$

$$J = Z\beta^* N_0 \exp\left(-\frac{\Delta G_c}{kT}\right), \quad (4)$$

where N_0 is the number of the nucleation sites, k is the Boltzmann constant, Z is the Zeldovich factor,³³ and β^* is the frequency of impurity atoms sticking to a critical nucleus.^{33,34}

In our previous work,⁹ the dependences of critical radius and the steady-state nucleation rate on the temperature for phosphorus precipitation in HP-Cz silicon were achieved according to Eqs. (2)–(4). Therein, ΔG_v was derived by using the Calculated Phase Diagram (CALPHAD) method and Scientific Group Thermodata Europe (SGTE) database.^{35–37} In the same way, the temperature-dependent critical radius and the steady-state nucleation rate for oxygen precipitation in Cz silicon can also be derived. To this end, the molar volume of oxide precipitates (V_{SiO_x} , $x \leq 2$) is adopted as $2.71 \times 10^{-5} \text{ m}^3$,³⁸ and the interfacial energy per unit area (γ) is take as 410 erg/cm^2 .¹⁵ While, according to Ref. 31, ΔG_v for oxygen precipitation can be derived from

$$\Delta G_v = \frac{\left((0.667 - x_O) \frac{\partial G_{Si,O}}{\partial x}|_{x=x_O} + G_{Si,O}|_{x=x_O}\right) - G_{SiO_x}}{V_{SiO_x}}. \quad (5)$$

In the above, G_{SiO_x} , the Gibbs free energy of oxide precipitate, can be calculated by³⁹

$$G_{SiO_x} = -4.4 \times 10^5 + 260T - 44.35T \ln T - 2.482 \times 10^{-3}T^2 + 1.2 \times 10^{-8}T^3 + 5.84 \times 10^5 T^{-1}. \quad (6)$$

Moreover, $G_{Si,O}$ is the Gibbs free energy of silicon solid solution containing oxygen impurities, which is expressed as

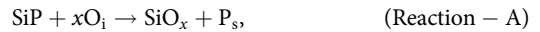
$$G_{Si,O} = x_O G_O + (1 - x_O) G_{Si} + RT[x_O \ln x_O + (1 - x_O) \ln(1 - x_O)], \quad (7)$$

where R is the gas constant and x_O is the atomic percentage of oxygen impurities in silicon. G_{Si} and G_O are, respectively, the Gibbs free energies of silicon matrix and oxygen impurities, which can be found in SGTE database.³⁷

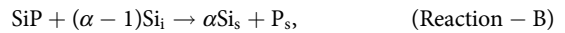
Figures 1(a) and 1(b) show the temperature-dependent critical radii and steady-state nucleation rates for phosphorus precipitation and oxygen precipitation. As can be seen, phosphorus precipitation exhibits a critical radius 1.5–2 times smaller and nucleation rates two to four orders of magnitude higher than oxygen precipitation across 850–1050 °C. Consequently, phosphorus precipitation exhibits higher thermodynamic propensity for nucleation under these conditions.

B. DFT calculations on the dissolution mechanisms of the SiP precipitate

As thermodynamically established above, the phosphorus impurities can precipitate more readily than the oxygen impurities in HP-Cz silicon. According to our previous work,⁹ the orthorhombic SiP precipitates form during the early stage anneal at the temperature of 850, 950, or 1050 °C investigated in this work. The evolution of these SiP precipitates during the prolonged anneal is supposed to involve two dissolution mechanisms. First, the interstitial oxygen (O_i) diffuses toward SiP precipitates. Given oxygen's higher Pauling electronegativity (3.44) vs phosphorus (2.19), oxidation of SiP precipitates occurs via Reaction-A,



where $x \leq 2$, and the generated phosphorus atoms are supposed to be substitutional, termed as P_s . In this way, the SiP precipitates could be gradually dissolved by the aforementioned oxidation. Second, oxygen precipitation occurs significantly during the prolonged isothermal anneal at each aforementioned temperature, emitting a number of interstitial silicon (Si_i) atoms.⁴⁰ Such emitted Si_i atoms will facilitate the dissolution of SiP precipitates via Reaction-B,



where Si_s represents the lattice silicon atom and α represents the ratio between the molar volumes of the silicon matrix and SiP. In this way, the SiP precipitates could be gradually dissolved along with the process of oxygen precipitation.

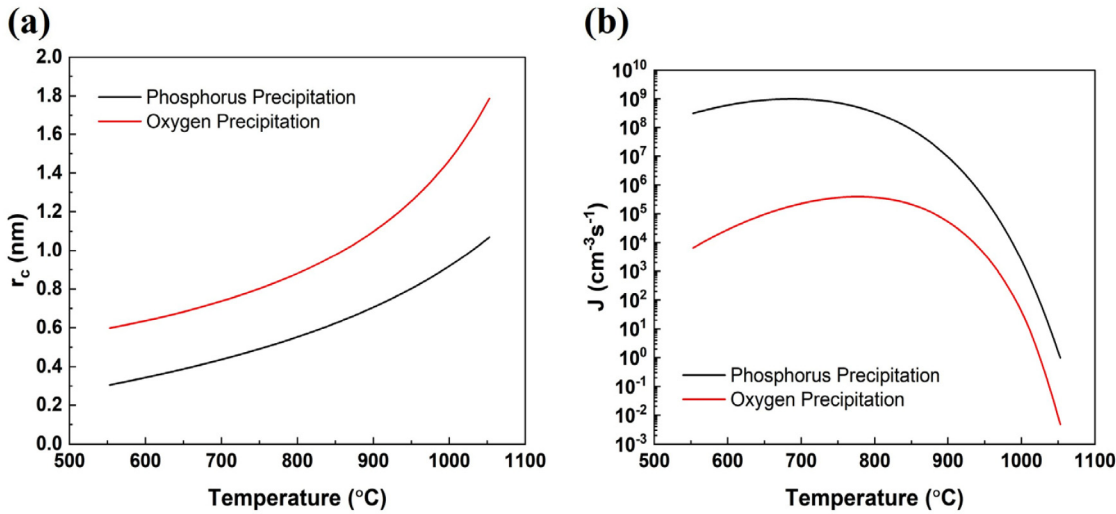


FIG. 1. (a) Critical radius and (b) steady-state nucleation rate as a function of temperature for phosphorus precipitation and oxygen precipitation in the HP-Cz silicon with a resistivity of $\sim 1 \text{ m}\Omega \cdot \text{cm}$.

In order to evaluate the change in energy (ΔE) for **Reactions-A** or **B**, we should resort to DFT calculations. To this end, an interface between a SiP precipitate and silicon matrix is constructed as mentioned earlier. Figure 2(a) shows the optimized structure of the supercell containing an interface between the orthorhombic SiP and the silicon diamond lattices. Herein, the orthorhombic SiP lattice contains 64 Si atoms and 64 P atoms, while the silicon diamond lattice contains 120 Si atoms. For **Reactions-A** or **B**, it proceeds via two sequential steps: (1) diffusion of an interstitial atom (O_i for **Reaction-A** and Si_i for **Reaction-B**) to the SiP/Si interface [step-I, Figs. 2(b) and 2(c)] and (2) subsequent substitution of a phosphorus atom at the interface by this diffused impurity atom [step-II, Figs. 2(d) and 2(e)]. Therefore, ΔE for **Reactions-A** or **B** is expressed as

$$\Delta E(x_i) = \Delta E_1(x_i) + \Delta E_2(x_i), \quad (8)$$

where x_i represents O_i for **Reaction-A** or Si_i for **Reaction-B**. ΔE_1 and ΔE_2 represent the energy changes for step-I (diffusion) and step-II (substitution), respectively. Furthermore, $\Delta E_1(x_i)$ and $\Delta E_2(x_i)$ can be calculated by a series of expressions as follows:

$$\Delta E_1(x_i) = \left(E_{Si_{184}P_{64}x_{i_2}} - E_{Si_{184}P_{64}} - 2 \times \mu_{x_i} \right) / 2 - E_f(x_i), \quad (9)$$

$$\Delta E_2(x_i) = \left(E_{Si_{184}P_{62}x_{i_2}} - E_{Si_{184}P_{64}x_{i_2}} + 2 \times \mu_P \right) / 2 + E_f(P_s^+), \quad (10)$$

$$E_f(O_i) = E_{Si_{216}O_i} - E_{Si_{216}} - \mu_O, \quad (11)$$

$$E_f(Si_i) = E_{Si_{216}Si_i} - E_{Si_{216}} - \mu_{Si}, \quad (12)$$

$$E_f(P_s^+) = E_{Si_{215}P_s^+} - E_{Si_{216}} + \mu_{Si} - \mu_P + (E_{VBM} + E_F) + E_{corr}. \quad (13)$$

In the above, $E_f(O_i)$, $E_f(Si_i)$, and $E_f(P_s^+)$ represent the formation energies for O_i atom, Si_i atom, and substitutional phosphorus ion (P_s^+) in the silicon matrix, respectively. μ_{Si} , μ_P , or μ_O is the chemical potential of a single silicon, phosphorus, or O atom. $E_{Si_{184}P_{64}}$, $E_{Si_{184}P_{64}x_{i_2}}$, and $E_{Si_{184}P_{62}x_{i_2}}$ represent the energy for: pristine SiP/Si interface [Fig. 2(a)]; the SiP/Si interface after diffusion of an interstitial atom from the Si matrix [Fig. 2(b) for O_i and Fig. 2(c) for Si_i]; and the SiP/Si interface following substitution of a P-atom by the diffused impurity atom [Fig. 2(d) for O_i and Fig. 2(e) for Si_i]. $E_{Si_{216}}$ represents the energy of the perfect Si_{216} supercell. $E_{Si_{216}O_i}$ or $E_{Si_{216}Si_i}$ represents the energy of the Si_{216} supercell containing an O_i atom or a Si_i atom. $E_{Si_{215}P_s^+}$ represents the energy of the supercell containing 215 Si lattice atoms and a P_s^+ ion. E_{VBM} denotes the energy of the valence band maximum. E_F represents the Fermi level. E_{corr} represents the charge-state dependent correction for a supercell with a finite size.^{41,42}

Based on all the expressions listed above, the DFT calculations indicate that (1) for **Reaction-A**, $\Delta E_1(O_i) = -0.989 \text{ eV}$ and $\Delta E_2(O_i) = 0.246 \text{ eV}$, then $\Delta E(O_i) = -0.743 \text{ eV}$. The negative $\Delta E_1(O_i)$ indicates the spontaneous aggregation of O_i atoms at the SiP/Si interface. In contrast, the positive $\Delta E_2(O_i)$ implies an energy barrier for step-II (phosphorus-atom substitution by O_i), establishing it as the rate-limiting step for the dissolution of SiP precipitates via **Reaction-A**; (2) for **Reaction-B**, $\Delta E_1(Si_i) = -3.461 \text{ eV}$ and $\Delta E_2(Si_i) = -0.151 \text{ eV}$, yielding $\Delta E(Si_i) = -3.611 \text{ eV}$, which is significantly lower than $\Delta E(O_i)$ of **Reaction-A**, indicating that **Reaction-B** is more thermodynamically favorable than **Reaction-A** to drive the dissolution of SiP precipitates. However, **Reaction-B** kinetics are critically limited by the availability of Si_i atoms emitted by oxygen precipitation.

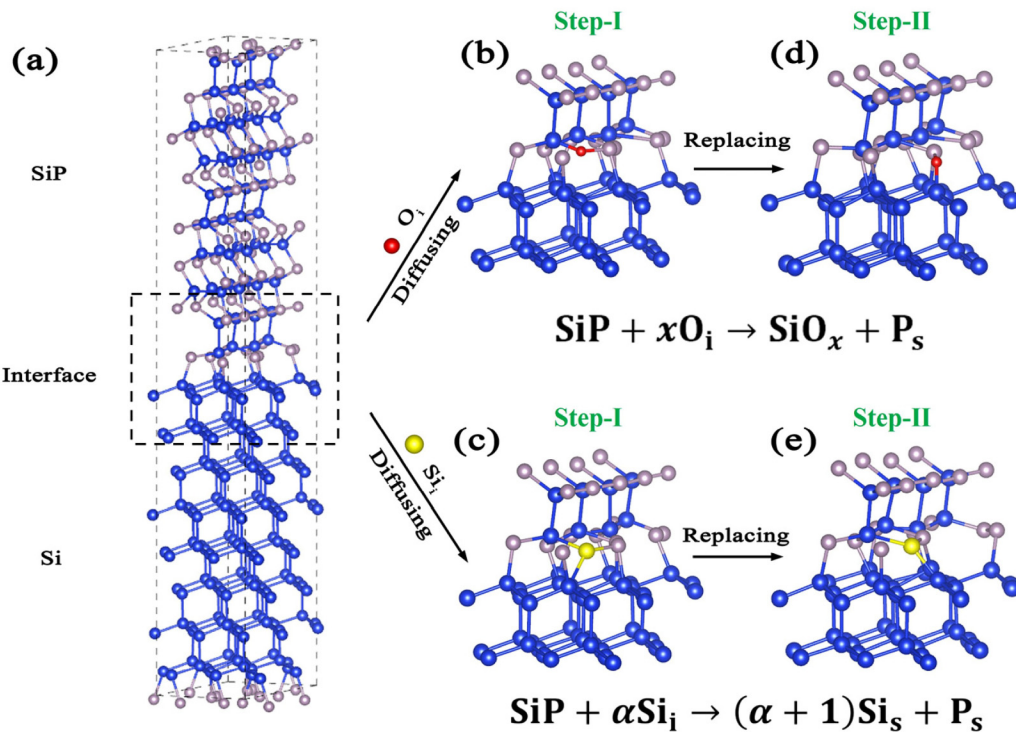


FIG. 2. The optimized structures of (a) a perfect SiP/Si interface, (b) and (c) the two SiP/Si interfaces into which an O_i and a Si_i atom, respectively, diffuse, and (d) and (e) the two SiP/Si interfaces where an O_i and a Si_i atom, respectively, replace a phosphorus atom. The spheres in blue, gray, red, and yellow denote Si, P, O_i , and Si_i atoms, respectively.

04 October 2025 06:19:18

C. Correlation between carrier concentration and precipitation behaviors

Figure 3 shows the evolutions of the precipitate density and the carrier (electron) concentration in the HP-Cz silicon specimens along with the annealing time at 850, 950, and 1050 °C, respectively. As seen, the precipitate density increases markedly during the early annealing stage (≤ 32 h at 850 °C, ≤ 16 h at 950 °C, or ≤ 4 h at 1050 °C), accompanied by a significant drop in carrier concentration. In our previous work,⁹ it has been clarified that phosphorus precipitation can occur during the early stage isothermal anneal at each of the aforementioned temperatures, forming numerous SiP precipitates. This leads to the electrical deactivation of a fraction of phosphorus impurities, reducing the carrier concentration. The above thermodynamic analyses have confirmed that phosphorus precipitation is more thermodynamically favorable than oxygen precipitation. Thus, the increase in precipitate density during the early-stage isothermal anneal is primarily attributed to phosphorus precipitation. Figure 3 further shows that as the annealing temperature increases, the maximum precipitate density due to phosphorus precipitation decreases, whereas the minimum carrier concentration increases. This trend stems from the progressively weaker phosphorus precipitation caused by the decreased supersaturation at higher temperatures.

Upon the prolonged anneal at each temperature (e.g., > 32 h at 850 °C), as shown in Fig. 3, the carrier concentration increases, indicating the dissolution of existing SiP precipitates, which releases the electrically active phosphorus impurities. In fact, oxygen precipitation may incubate during the early stage anneal at each temperature. With the extension of isothermal anneal, oxygen precipitation becomes increasingly significant. In Fig. 3, a distinct transition period (32–64 h at 850 °C, 16–32 h at 950 °C, or 4–16 h at 1050 °C) exhibits the decreasing precipitate density alongside the increasing carrier concentration. This occurs because the dissolved SiP precipitates exceed the newly formed oxide precipitates. Beyond this period, the precipitate density increases again with the annealing time up to 128 h due to the dominant oxygen precipitation. Notably, after 128 h anneal at 850 °C, the carrier concentration remains below its initial value, suggesting the permanent incorporation of phosphorus impurities into the oxide precipitates. In contrast, nearly full recovery of carrier concentration occurs after 128 h anneal at 950 °C or 16 h anneal at 1050 °C, implying that nearly all the phosphorus impurities released from the dissolved SiP precipitates revert to be electrically active.

In a word, Fig. 3 reveals the competing precipitation behaviors of phosphorus and oxygen in HP-Cz silicon during the prolonged anneal at 850, 950, or 1050 °C, through the correlated evolutions of carrier concentration and impurity precipitation. While our

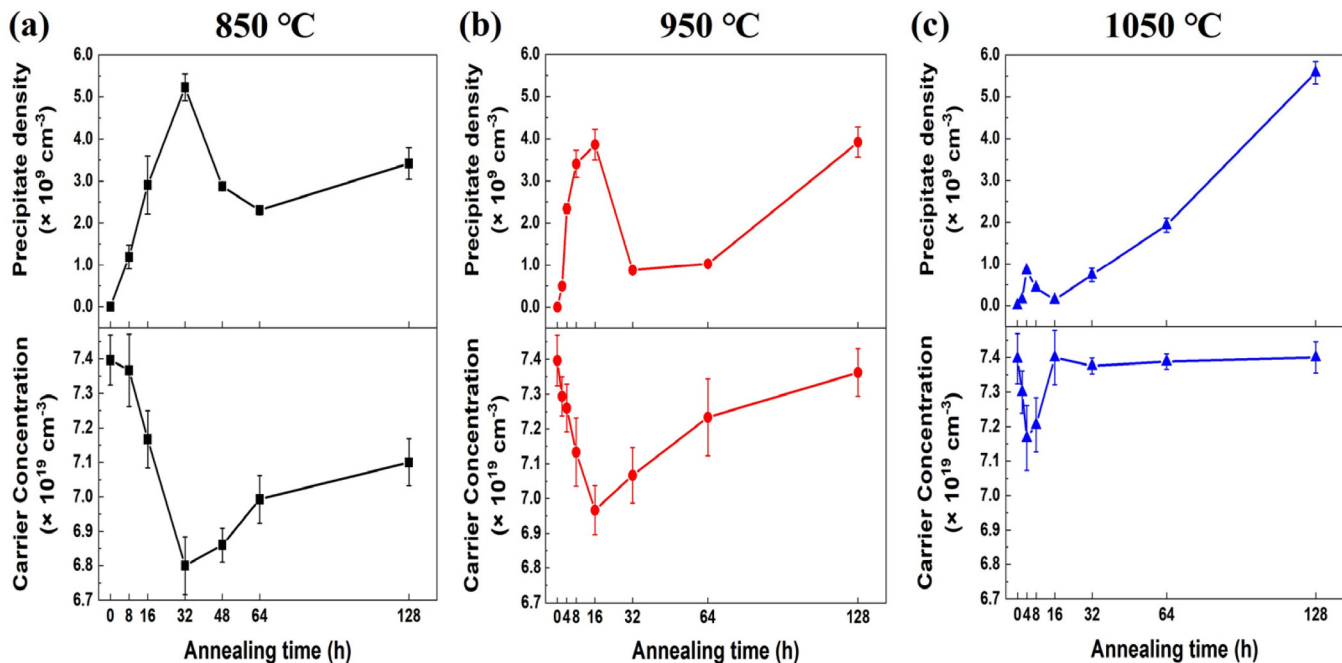


FIG. 3. Dependences of precipitate density and carrier concentration in HP-Cz silicon on the annealing time at (a) 850, (b) 950, and (c) 1050 °C.

04 October 2025 / 0619-18

previous work has elucidated the early-stage phosphorus precipitation mechanism at these temperatures,⁹ herein, we employ TEM to directly track the evolution of oxygen precipitation during the extended anneal for up to 128 h. This aims to reveal how the oxide precipitate nucleation/growth and the phosphorus incorporation govern the late-stage precipitation behaviors and carrier concentration recovery.

D. TEM characterization on oxygen precipitation

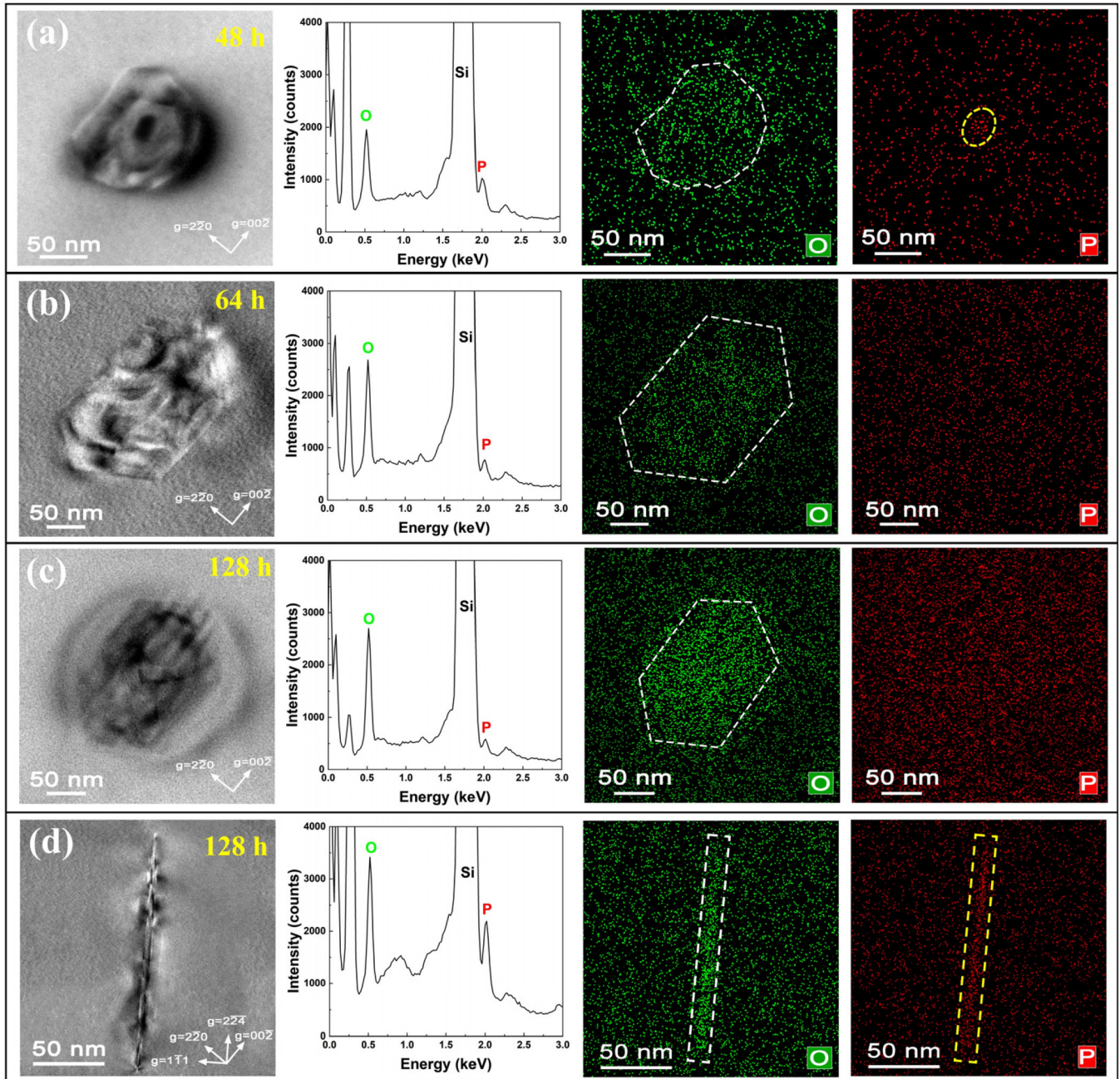
1. 850 °C anneal

Figure 4 shows the representative TEM images of the precipitates formed in the HP-Cz silicon specimens annealed at 850 °C for 48–128 h, as well as the EDS spectra and the EDS mapping images of oxygen and phosphorus elements. Figure 4(a) illustrates an observed core-shell-like precipitate in the 48 h-annealed specimen. This structure exhibits a central core with strong image contrast against the surrounding hexagonal shell. The acquired EDS spectrum exhibits prominent signals of phosphorus and oxygen elements. In the phosphorus EDS mapping image, the yellow dashed contour corresponding to the aforementioned central core displays the phosphorus impurity aggregation, which is believed to result in a SiP precipitate according to our previous work.⁹ While, in the oxygen EDS mapping image, the white dashed contour corresponding to the aforementioned surrounding hexagonal shell indicates the precipitation of oxygen impurities. Collectively, Fig. 4(a) demonstrates oxygen precipitation heterogeneously nucleated on the SiP precipitate. As revealed in Fig. 3(a), phosphorus precipitation dominates in HP-Cz silicon during the initial 32 h anneal at

850 °C, beyond which oxygen precipitation becomes increasingly significant. Therein, the preformed SiP precipitates provide heterogeneous nucleation sites for oxygen precipitation during the subsequent annealing. For the specimens annealed for 48 h and beyond, the SiP precipitates were rarely observed while the oxide precipitates were frequently found by TEM. Figures 4(b) and 4(c) show the representative TEM images, EDS spectra, and elemental mapping images of the “hexagonal” oxide precipitates formed in the two specimens annealed for 64 and 128 h, respectively. As revealed by the EDS spectra and images, the prolonged anneal enhances oxygen precipitation, yet discernible phosphorus signals persist, indicating the phosphorus incorporation into the oxide precipitates. Therefore, it is understandable that the carrier concentrations in such two specimens fail to recover to the initial level, as shown in Fig. 3(a).

It should be pointed out that the “hexagonal” oxide precipitates as shown in Figs. 4(a)–4(c) lie flat on the TEM observation plane [i.e., the (110) plane]. Actually, such oxide precipitates are plate-like, which was derived from the TEM observations through titling the specimens. It has been well documented that the oxide precipitates formed at the temperatures lower than 1000 °C in Cz silicon generally adopt the platelet morphologies to minimize the strain energy.^{15,43,44} In reality, in the 128 h-annealed specimen, Fig. 4(d) reveals a platelet oxide precipitate intersecting the TEM observation plane. Moreover, the EDS data indicate that a number of phosphorus impurities are incorporated into the oxide precipitate, thus losing electrical activity.

Based on Figs. 1, 3(a), and 4, the gradual dissolution of the SiP precipitates formed by the initial 32 h anneal at 850 °C during



04 October 2025 06:19:18

FIG. 4. The representative TEM images, EDS spectra, and mapping images of oxygen and phosphorus elements for the precipitates formed in the HP-Cz silicon specimens annealed at 850 °C for (a) 48, (b) 64, and (c) and (d) 128 h. The white dashed contours in oxygen maps highlight the precipitated regions, while the yellow dashed contours in phosphorus maps indicate the precipitation sites.

the prolonged anneal is mechanistically described below. As Fig. 1 demonstrates, the nucleation rate of phosphorus precipitation exceeds that of oxygen precipitation by three orders of magnitude, and the critical radius for phosphorus precipitation is significantly

smaller. Consequently, oxygen precipitation is negligible within the initial 32 h of 850 °C anneal. During the prolonged 850 °C anneal, the oxygen impurities diffuse to the SiP/Si interfaces, triggering Reaction-A (as mentioned in Sec. IV B) that oxidizes the SiP

precipitates thus resulting in the dissolution of SiP precipitates. Such gradual dissolution of SiP precipitates releases the phosphorus impurities, restoring their electrical activity manifested by the increase in carrier concentration, as shown in Fig. 3(a). Concurrently, the oxide precipitates heterogeneously nucleate on the shrinking SiP precipitates, as directly visualized in Fig. 4(a). As the anneal progresses, the oxide precipitates coarsen while the SiP precipitates progressively diminish until complete dissolution. During the early-stage dissolution of SiP precipitates, the released phosphorus impurities readily occupy the silicon lattice sites, regaining the electrical activity. Following the heterogeneous oxide formation on the dissolving SiP precipitates, the interstitial oxygen atoms in the silicon matrix should diffuse through the oxide (SiO_x) layer to reach the residual SiP precipitates, thus activating Reaction-A. Herein, the phosphorus impurities released from the dissolution of residual SiP precipitates are predominantly trapped within the oxide precipitates due to the sluggish phosphorus diffusion at 850 °C. Although Reaction-A dominates the SiP precipitate dissolution, Reaction-B (as mentioned in Sec. IV B) will contribute secondarily when the oxide precipitates grow large enough to emit Si_i atoms.

2. 950 °C anneal

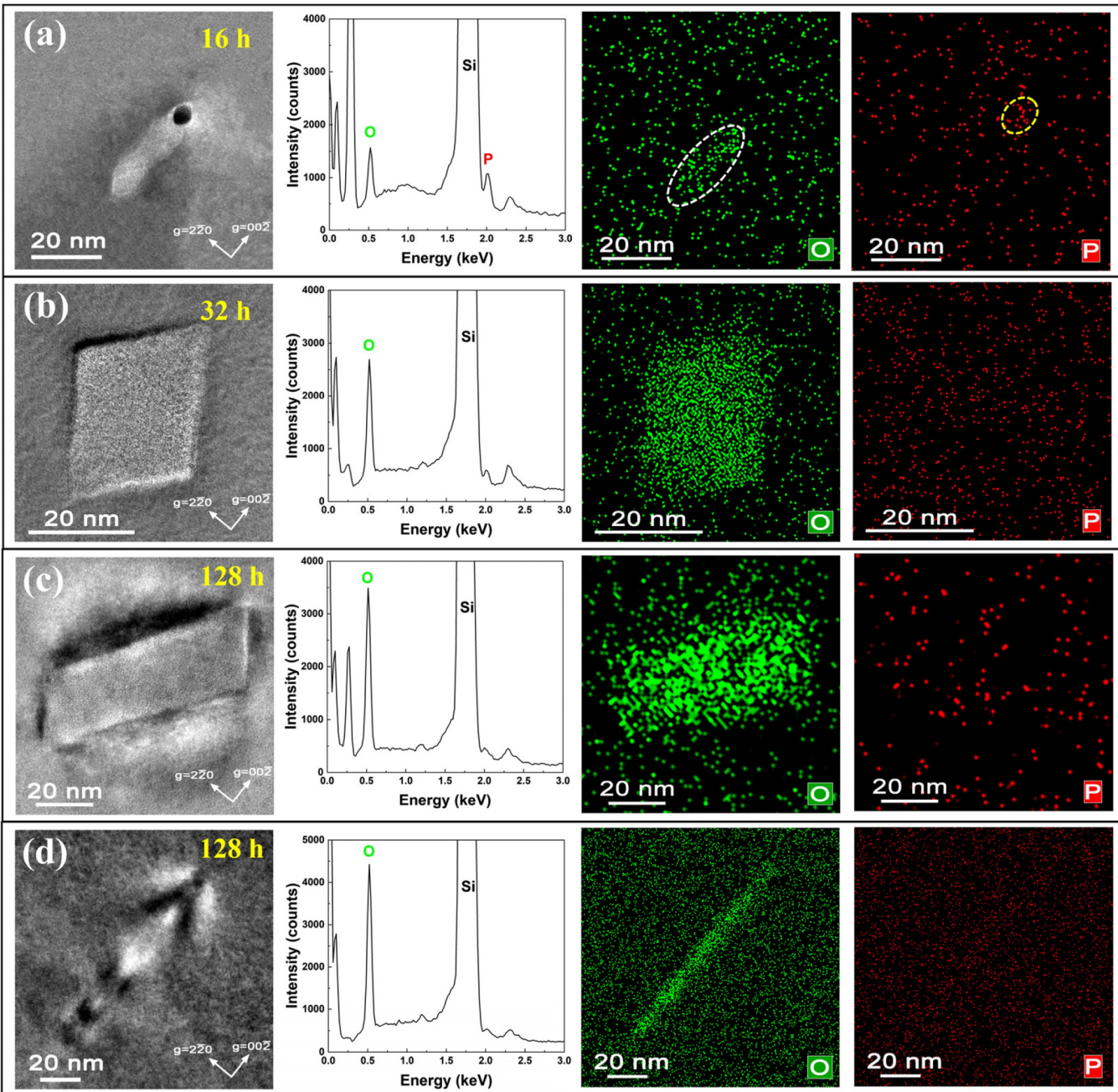
Figure 5 shows the representative TEM images of the oxide precipitates formed in the HP-Cz specimens annealed at 950 °C for 16–128 h, together with the corresponding EDS spectra and elemental mapping images. The integrated analysis of Fig. 5(a) (TEM image, EDS spectrum, and P/O elemental mapping images) confirms the heterogeneous nucleation of an oxide precipitate on a SiP precipitate, demonstrating that oxygen precipitation has occurred during the initial 16 h anneal at 950 °C. However, Fig. 3(b) shows the maximum precipitate density and the minimum carrier concentration at 16 h of 950 °C anneal. Thus, despite the onset of oxygen precipitation, phosphorus precipitation remains dominant during this period. In the 32 h-annealed specimen, Fig. 5(b) illustrates a quadrangular-shaped oxygen precipitate and the TEM observation through tilting the specimen confirmed its plate-like morphology, similar to the square-shaped oxide precipitate platelets reported by Wijaranakula.⁴⁵ The EDS mapping shows the significant oxygen aggregation without discernible phosphorus aggregation. Notably, the oxygen aggregation intensity in this quadrangular platelet exceeds that in the hexagonal platelets as shown in Fig. 4. This is attributed to the relatively larger thickness of quadrangular platelets, as confirmed by the tilting TEM observations. Figure 5(c) shows a larger quadrangular platelet oxide precipitate with {110} habit planes and {001} edges in the 128 h-annealed specimen. For a plate-like precipitate parallel to the (110) plane, a cross section perpendicular to [001] would display a rectangular morphology featuring {110} habit planes and edges along both {001} and {110} directions. This configuration is directly confirmed in Fig. 5(d). Furthermore, the EDS spectra and elemental mapping image in Figs. 5(c) and 5(d) demonstrate negligible incorporation of phosphorus impurities into the oxide precipitates. This result is consistent with the recovery of carrier concentration to its initial value after 128 h anneal as shown in Fig. 3(b).

During the prolonged anneal at 950 °C, the dissolution of SiP precipitates driven by oxygen precipitation follows a scenario largely similar to that at 850 °C. However, due to the significantly higher diffusivities of both oxygen and phosphorus impurities at 950 °C, the SiP precipitate dissolution mediated by Reaction-A is accelerated and the escape of released phosphorus from the growing oxide precipitates is enhanced. Moreover, the dissolution of SiP precipitates via Reaction-B also intensifies at 950 °C owing to the enhanced emission of Si_i atoms from the oxide precipitates. Consequently, the carrier concentration in HP-Cz silicon recovers nearly to its initial value after 128 h anneal at 950 °C, as shown in Fig. 3(b).

3. 1050 °C anneal

Figure 6 shows the representative TEM images, EDS spectra, and elemental mapping of oxygen and phosphorus elements for the precipitates formed in the HP-Cz specimens annealed at 1050 °C for 8–128 h. As confirmed by the EDS spectra and elemental mapping images, the observed precipitates are of oxide precipitates with no discernible phosphorus incorporation. Figure 6(a) illustrates an oxide precipitate in the 8 h-annealed specimen, exhibiting no heterogeneous nucleation on the SiP precipitate. Figure 6(b) reveals a well-defined octahedral oxide precipitate in the 16 h-annealed specimen. This precipitate exhibits sharp edges with the symmetry axes aligned along the [002] and [220] orientations of the silicon matrix in the viewing plane. Actually, the TEM observations via tilting the specimen confirmed the polyhedral morphology of the observed oxide precipitate. Moreover, the EDS mapping image shows the oxygen intensity stronger in the precipitate's center, decreasing progressively toward both ends along the [002] direction, indicating the larger thickness at the center. This evidences the polyhedral nature of the oxide precipitate. Figures 6(c) and 6(d) illustrate the truncated octahedral oxide precipitates formed in the specimens annealed for 32 and 128 h, respectively. Through a series of TEM observations, the progressive truncation of octahedral precipitate at both ends was revealed. In the specimen annealed for 32 or 64 h, the single-sided truncated octahedral oxide precipitates were predominantly observed, while only the double-sided truncated octahedral precipitates were found in the specimen annealed for 128 h.

Although the heterogeneous nucleation of oxide precipitates on the SiP precipitates is not observed in Fig. 6, this mechanism cannot be ruled out. As shown in Fig. 3(c), during the initial 4 h anneal at 1050 °C, a number of SiP precipitates have formed, leading to the decrease in carrier concentration. According to our previous work,⁹ the sphere-like SiP precipitate with a radius of ~5 nm in the 1050 °C/4 h-annealed HP-Cz silicon specimen was observed by TEM. Consequently, the heterogeneous nucleation of oxygen precipitation on the existing SiP precipitates becomes thermodynamically favorable. The high oxygen diffusivity at 1050 °C enables the significant oxygen diffusion to the SiP/Si interfaces, facilitating the oxidation of SiP precipitates. This initiates oxygen precipitation on the existing SiP precipitates. Along with the coarsening of oxide precipitates, the SiP precipitates are progressively dissolved via aforementioned Reaction-A. The dissolution of SiP precipitates mediated by Reaction-A proceeds much more rapidly at 1050 °C than at 850 and 950 °C. Hence, the TEM detection of



04 October 2025 06:19:18

FIG. 5. The representative TEM images, EDS spectra, and mapping images of oxygen and phosphorus elements for the precipitates formed in the HP-Cz silicon specimens annealed at 950 °C for (a) 16, (b) 32, and (c) and (d) 128 h. The white dashed contour in oxygen map highlights the precipitated region, while yellow dashed contour in phosphorus map indicates precipitation site.

heterogeneous oxide precipitate nucleation on the existing SiP precipitates in the 1050 °C-annealed specimen is extremely challenging. Additionally, the dissolution of SiP precipitates mediated by Reaction-B may occur concurrently. After all, oxygen precipitation

at 1050 °C could be simultaneously enabled by alternative heterogeneous nucleation mechanism. It is well documented that the emission of Si_i atoms becomes more significant due to oxygen precipitation at high temperatures.⁴⁶ Under such conditions, the

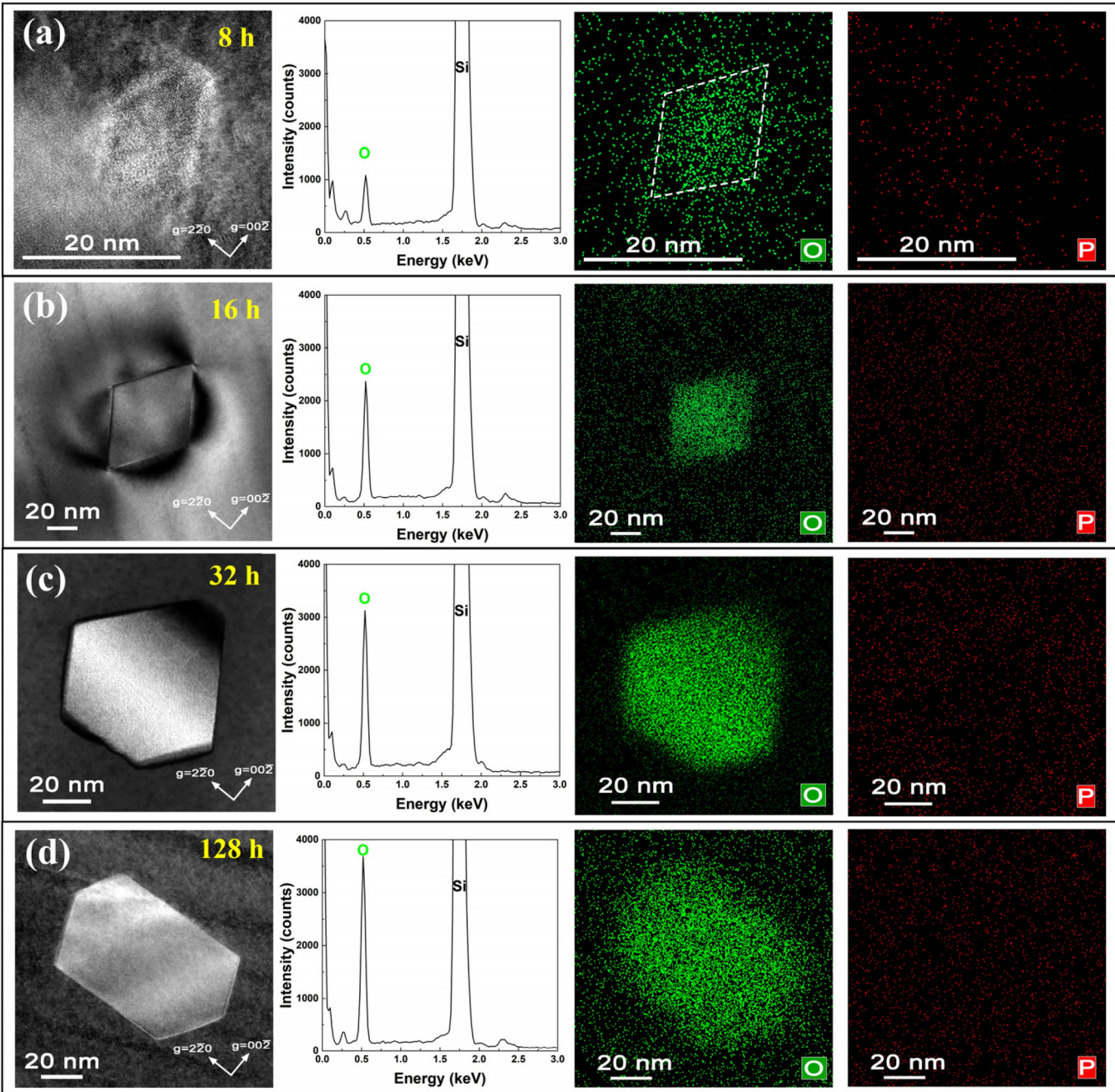


FIG. 6. The representative TEM images, EDS spectra, and mapping images of oxygen and phosphorus elements for the precipitates formed in the HP-Cz silicon specimens annealed at 1050 °C for (a) 8, (b) 16, (c) 32, and (d) 128 h.

04 October 2025 06:19:18

excess Si_i atoms drive the Reaction-B-mediated dissolution of SiP precipitates. In a word, at 1050 °C, oxygen-precipitation-induced dissolution of SiP precipitates proceeds more rapidly; concurrently, the released phosphorus impurities readily incorporate into the

silicon lattice sites to regain the electrical activity. Consequently, the carrier concentration in HP-Cz silicon recovers to its initial value after 16 h anneal at 1050 °C [Fig. 3(c)], essentially due to the aforementioned phosphorus reactivation.

V. CONCLUSIONS

In summary, we have comprehensively investigated the competing precipitation behaviors of phosphorus and oxygen in HP-Cz silicon subjected to the prolonged anneal at 850–1050 °C. Based on the changes in carrier concentrations in the annealed HP-Cz silicon specimens and on the rigorous thermodynamic analyses, it is derived that the phosphorus impurities exhibit faster precipitation than the oxygen impurities. Consequently, during the early annealing stages, the substitutional phosphorus impurities are partially consumed by the faster phosphorus precipitation, leading to the decrease in carrier concentration. Along with the extension of isothermal anneal at each temperature, oxygen precipitation becomes increasingly significant while the preformed SiP precipitates are progressively dissolved, resulting in the gradual recovery of carrier concentration. The carrier concentration recovers nearly completely after 128 h at 950 °C or 16 h at 1050 °C, but fails to recover fully even after 128 h at 850 °C due to the phosphorus trapping in the oxide precipitates. Regarding the nucleation of oxygen precipitation, while it predominantly occurs on the preformed SiP precipitates, which is directly visualized by TEM in the case of 850 or 950 °C anneal, alternative heterogeneous pathways and even the homogeneous nucleation may coexist. The systematic TEM characterizations reveal the temperature-dependent morphological evolution of the oxide precipitates. As the annealing temperature increases, the oxide precipitates transition from hexagonal platelet to quadrangular platelet and ultimately adopt octahedral (or truncated octahedral) geometries, reflecting the energy-minimization principles. This work has well elucidated the competitive thermodynamics and kinetics between phosphorus precipitation and oxygen precipitation during the thermal processing of HP-Cz silicon wafers, providing fundamental insights into the temporal and thermal dependencies of impurity precipitation behaviors in Cz silicon.

ACKNOWLEDGMENTS

This work was supported by the Natural Science Foundation of China (NSFC) (Grant No. 62174145) and the Natural Science Foundation of Zhejiang (No. LZ25E070001).

AUTHOR DECLARATIONS

Conflict of Interest

The authors have no conflicts to disclose.

Author Contributions

Defan Wu and Tong Zhao contributed equally to this paper.

Defan Wu: Data curation (lead); Formal analysis (equal); Methodology (equal); Visualization (lead); Writing – original draft (equal). **Tong Zhao:** Formal analysis (equal); Validation (equal); Writing – original draft (equal). **Xingbo Liang:** Data curation (equal); Methodology (equal); Resources (equal). **Tianqi Deng:** Data curation (equal); Formal analysis (equal); Methodology (lead). **Hao Chen:** Data curation (equal); Validation (equal). **Qunlin Nie:** Data curation (equal); Validation (equal). **Bin Ye:** Data curation (equal); Resources (equal); Validation (equal). **Shenzhong Li:** Data

curation (equal); Validation (equal). **Daxi Tian:** Data curation (equal); Resources (equal). **Deren Yang:** Resources (lead); Supervision (equal); Writing – review & editing (equal). **Xiangyang Ma:** Conceptualization (lead); Funding acquisition (lead); Resources (lead); Supervision (lead); Writing – review & editing (lead).

DATA AVAILABILITY

The data that support the findings of this study are available from the corresponding author upon reasonable request.

REFERENCES

- ¹H. D. Chiou, *J. Electrochem. Soc.* **147**(1), 345 (2000).
- ²M. Hourai, Y. Narushima, K. Torigoe, N. Nonaka, K. Koga, T. Ono, H. Horie, and K. Sueoka, *J. Appl. Phys.* **136**(5), 055706 (2024).
- ³H. Koder, *Jpn. J. Appl. Phys.* **2**(9), 527 (1963).
- ⁴D. Nobili, A. Armigliato, M. Finnetti, and S. Solmi, *J. Appl. Phys.* **53**(3), 1484 (1982).
- ⁵J. Friedrich, L. Stockmeier, and G. Müller, *Acta Phys. Pol. A* **124**(2), 219 (2013).
- ⁶L. Morettini and D. Nobili, *Mater. Chem. Phys.* **10**(1), 21 (1984).
- ⁷G. Stingeder, P. Pongratz, W. Kuhnert, and T. Brabec, *Fresen. Z. Anal. Chem.* **333**(3), 191 (1989).
- ⁸S. Solmi, A. Parisini, R. Angelucci, A. Armigliato, D. Nobili, and L. Moro, *Phys. Rev. B* **53**(12), 7836 (1996).
- ⁹D. Wu, T. Zhao, B. Ye, H. Chen, X. Liang, S. Li, D. Tian, D. Yang, and X. Ma, *J. Appl. Phys.* **134**(15), 5701 (2023).
- ¹⁰L. Stockmeier, M. Elsayed, R. Krause-Rehberg, M. Zschorsch, L. Lehmann, and J. Friedrich, *Solid State Phenom.* **242**(10), 10 (2015).
- ¹¹Z. Zeng, X. Ma, J. Chen, D. Yang, I. Ratschinski, F. Hevrot, and H. S. Leipner, *J. Cryst. Growth* **312**(2), 169 (2010).
- ¹²I. Yonenaga and K. Sumino, *J. Appl. Phys.* **80**(2), 734 (1996).
- ¹³I. Yonenaga, K. Sumino, and K. Hoshi, *J. Appl. Phys.* **56**(8), 2346 (1984).
- ¹⁴G. Kissinger, *Defects and Impurities in Silicon Materials: An Introduction to Atomic-Level Silicon Engineering* (Springer, 2015), p. 293.
- ¹⁵A. Borghesi, B. Pivac, A. Sassella, and A. Stella, *J. Appl. Phys.* **77**(9), 4169 (1995).
- ¹⁶K. B. Willardson, E. R. Weber, A. C. Beer, and F. Shimura, *Oxygen in Silicon* (Academic Press, 1994), p. 55.
- ¹⁷R. Newman, *J. Phys.: Condens. Matter* **12**(25), R335 (2000).
- ¹⁸S. Hu, *MRS Online Proc. Libr.* **59**, 249 (1985).
- ¹⁹S. Hu, *J. Appl. Phys.* **52**(6), 3974 (1981).
- ²⁰Y. Zeng, D. Yang, X. Ma, J. Chen, and D. Que, *Mater. Sci. Eng. B* **159–160**, 145 (2009).
- ²¹Y. Zeng, D. Yang, X. Ma, X. Zhang, L. Lin, and D. Que, *ECS Trans.* **18**(1), 1001 (2009).
- ²²S. Matsumoto, I. Ishihara, H. Kaneko, H. Harada, and T. Abe, *Appl. Phys. Lett.* **46**(10), 957 (1985).
- ²³Y. Zeng, X. Ma, D. Tian, W. Wang, L. Gong, D. Yang, and D. Que, *J. Appl. Phys.* **105**(9), 3503 (2009).
- ²⁴M. Porrini, J. Duchini, and A. Bazzali, *Cryst. Res. Technol.* **49**(8), 564 (2014).
- ²⁵K. Sueoka, Y. Narushima, K. Torigoe, N. Nonaka, K. Koga, T. Ono, H. Horie, and M. Hourai, *J. Appl. Phys.* **136**(5), 0055705 (2024).
- ²⁶P. Pichler, *Intrinsic Point Defects, Impurities, and Their Diffusion in Silicon* (Springer Science & Business Media, Berlin, 2012).
- ²⁷G. Kresse and J. Furthmüller, *Phys. Rev. B* **54**(16), 11169 (1996).
- ²⁸T. Zhao, D. Wu, W. Lan, D. Yang, and X. Ma, *J. Appl. Phys.* **131**(15), 5703 (2022).
- ²⁹K. Momma and F. Izumi, *J. Appl. Crystallogr.* **44**(6), 1272 (2011).
- ³⁰K. C. Russell, *Adv. Colloid Interface Sci.* **13**(3–4), 205 (1980).

04 October 2025 / 06:19:18

- ³¹R. Wagner, R. Kampmann, and P. W. Voorhees, in *Phase Transformations in Materials* (Wiley-VCH Verlag GmbH, Weinheim, 2001), p. 314.
- ³²T. Y. Tan and W. J. Tylor, in *Semiconductors and Semimetals: Oxygen in Silicon* (Academic Press, New York, 1994), p. 353.
- ³³Y. B. Zeldovich, *Acta Physicochem. USSR* **18**(1), 1 (1943).
- ³⁴J. Svoboda, F. Fischer, P. Fratzl, and E. Kozeschnik, *Mater. Sci. Eng. A* **385**(1), 166 (2004).
- ³⁵W. Cao, S.-L. Chen, F. Zhang, K. Wu, Y. Yang, Y. Chang, R. Schmid-Fetzer, and W. Oates, *Calphad* **33**(2), 328 (2009).
- ³⁶Y. A. Chang, S. Chen, F. Zhang, X. Yan, F. Xie, R. Schmid-Fetzer, and W. A. Oates, *Prog. Mater. Sci.* **49**(3–4), 313 (2004).
- ³⁷A. T. Dinsdale, *Calphad* **15**(4), 317 (1991).
- ³⁸R. K. Willardson, E. R. Weber, A. C. Beer, and F. Shimura, *Oxygen in Silicon* (Academic Press, 1994), p. 176.
- ³⁹S. Schnurre, J. Gröbner, and R. Schmid-Fetzer, *J. Non-Cryst. Solids* **336**(1), 1 (2004).
- ⁴⁰G. Kissinger, D. Kot, and A. Sattler, *ECS J. Solid State Sci. Technol.* **13**(8), 083005 (2024).
- ⁴¹C. Freysoldt, J. Neugebauer, and C. G. Van de Walle, *Phys. Rev. Lett.* **102**(1), 016402 (2009).
- ⁴²S. E. Taylor and F. Bruneval, *Phys. Rev. B Condens. Matter Mater. Phys.* **84**(7), 075155 (2011).
- ⁴³D. Kot, G. Kissinger, M. A. Schubert, and A. Sattler, *ECS Trans.* **64**(11), 71 (2014).
- ⁴⁴G. Kissinger, D. Kot, A. Huber, R. Kretschmer, T. Müller, and A. Sattler, *ECS J. Solid State Sci. Technol.* **9**(6), 064002 (2020).
- ⁴⁵W. Wijaranakula, *J. Appl. Phys.* **72**(9), 4026 (1992).
- ⁴⁶K. Torigoe and T. Ono, *J. Appl. Phys.* **121**(21), 215103 (2017).